Supporting Information

Shafer et al. 10.1073/pnas.1711652115

Synthesis and Structural Characterization

Superlattices of $(SrTiO_3)/(PbTiO_3)$ were synthesized on $DyScO_3$ $(110)_O$ substrates by pulsed laser deposition at a set temperature of 630 °C and growth pressure of 100 mTorr. While the growth of $PbTiO_3$ was achieved using a lead-rich polycrystalline target with composition $Pb_{1.2}TiO_3$, growth of $SrTiO_3$ was done using a single crystalline target. For the growth of superlattice films, a buffer layer of $SrRuO_3$ was used which was grown at a set temperature of 700 °C and growth pressure of 50 mTorr. A laser fluence of 1.5 J/cm^2 was used on all three targets. The growth of $PbTiO_3$ and $SrTiO_3$ was monitored throughout using intensity oscillations in the RHEED pattern along the $[\bar{1}10]_O$ direction of the $DyScO_3$ substrate near the specular reflection. After growth, films were cooled at an oxygen pressure of 50 Torr to ensure full oxidation of the samples. This growth process is identical to that used in ref. 5 to synthesize $(SrTiO_3)/(PbTiO_3)$ superlattices, and samples were similarly characterized by XRD, RBS, and TEM to reveal the structure and chemical homogeneity of superlattice films.

RSXD Measurements

Synchrotron-based RSXD experiments were performed at the Advanced Light Source, using the scattering endstation at beamline 4.0.2. Polarization and photon energy of the X-ray source were tuned by an elliptically polarizing undulator. Intensities of X-rays scattered by the sample were measured using an in-vacuum 1,024 × 1,024 pixel CCD that is sensitive to soft X-rays. Background dark counts were removed by subtracting "dark images" (images captured without X-ray exposure) that were measured for the same duration as data images.

Resonance profiles were measured by tuning the photon energy through the titanium $L_{3,2}$ edges (~450 eV to 470 eV), while sample and detector angles were adjusted to maintain the Bragg condition for each energy. Unless otherwise noted, the azimuth of the diffraction spot (ϕ_{spot}) was set near +90° to maximize the signal. X-ray absorption spectra were measured by the fluorescence detected in the peripheral regions of the CCD (away from the diffraction spot). Every spectrum was collected as a pair of curves with oppositely polarized X-ray helicity. I_0 was recorded at each photon energy and helicity, by measuring the drain current of a gold mesh upstream of the sample during the collection of every dataset. All spectra were normalized as follows. For each X-ray polarization, the measured fluorescence or scattered intensity was divided by I_0 at each photon energy to correct for the energy dependence of the incoming photon flux. To account for the slight imperfection of this approach, resulting curves were scaled to the same value in the featureless photon energy range of the preedge region. For data plotted in Figs. 1*C*, *Upper* and 4, *Upper*, the intensity in the preedge region was assigned the value "0," and the most intense feature of the polarization-averaged spectrum (i.e., averaged over the two X-ray helicities) was set equal to 1.

XCD was calculated for resonance profiles and reciprocal space line cuts as the difference of the scattered intensity for the two curves measured with opposite helicity of circularly polarized X-rays. Curves were normalized as described above, allowing XCD to be compared meaningfully between datasets as a fraction of the average scattered intensity. The term "dichroism" more strictly refers to a difference in absorption, so that a difference in reflectivity or diffraction for circularly polarized light is more generally referred to as the "circular difference." We have chosen to use the broader definition of XCD to include both absorptive and refractive effects, as is common in the literature.

Phase Coexistence

TEM and piezoresponse force microscopy indicate that the chiral polar phase coexists with ferroelectric a_1/a_2 domains in $(PbTiO_3)_n/(SrTiO_3)_n$ superlattices for $n = 10$ to 16. Cross-sectional and planar view TEM show that these two phases segregate into mesoscale regions of chiral textures that neighbor regions of *a* domains. RSXD can distinguish between these phases owing to their distinct periodicities and ordering directions, as illustrated in Fig. S2. The chiral textures order along the principal pseudocubic axes of the substrate, $[100]_{pc}$ or $[010]_{pc}$, whereas the *a* domains order along pseudocubic in-plane diagonals, $[110]_{pc}$ or $[1\bar{1}0]_{pc}$, with a moderately wider domain period. In this way, the diffraction signal from the chiral polar phase can be readily isolated.

XCD of Ordered Phases

The spectra in Fig. S2 show that, while XCD is strong (typically ~20%) in the chiral diffraction peaks, it is only a few percent (of the polarization-averaged diffraction intensity) for the *a*-domain peaks measured in the same sample. This small XCD is likely an indication of coupling that occurs at the many interfaces between regions of chiral polar order and *a* domains. Any XCD that might be present in the *a*-domain peaks is further reduced to the level of uncertainty in the measurement of $n = 4$ superlattices, which exhibit no chiral polar arrays but have periodic arrays of in-plane-oriented, ferroelectric *a* domains with a period of ~70 nm. No appreciable XCD was found in the *a*-domain peaks of the $n = 4$ superlattices at any azimuth. To first order, we expect dynamical scattering effects (19–21, 24) to be similar in both the $n = 4$ (*a* domain) and $n = 14$ (chiral) superlattices, given their similar chemical composition and because both samples are strongly polar. Their key distinction is that chiral textures form in $n = 14$ superlattices but not in $n = 4$ superlattices. Thus, the dramatic difference in XCD between samples with and without curled polar textures directly points to their chiral structure rather than dynamical effect as the primary origin of XCD. Finally, it seems likely that XCD from the chiral polar arrays could increase considerably (as a fraction of the diffraction intensity) if samples could be fabricated with pure chiral texture, free of classical *a* domains.

The XCD map in Fig. 1*D* shows a large contiguous region near the top edge having positive XCD (red), indicative of the same polar helicity that is responsible for XCD in Figs. 1 *B* and *C* and 3, whereas negative XCD (blue) in the contiguous region near the bottom edge denotes a large portion of the sample in which the opposite helicity exists instead. The size of these iso-chiral macrodomains far exceeds the mesoscale phase separation distances (~300 nm) between chiral polar and *a*-domain phases. This suggests that the phases must interact cooperatively to provide extended regions (millimeter scale) in which the axial polarization is "communicated" across the phase boundaries.

ATS Diffraction

Diffraction from the chiral polar arrays in $PbTiO_3/SrTiO_3$ superlattices occurs due to a mechanism known as ATS scattering (15, 16). ATS diffraction peaks were observed near resonant electronic transitions using soft X-rays in proximity to the titanium $L_{3,2}$ (~450 eV to 470 eV) and oxygen K (~520 eV to 540 eV) absorption edges. Only near resonant transitions are the X-rays sensitive to the anisotropic electronic structure of the distorted

TiO_6 octahedra. These distortions lead to pronounced XLD in the absorption spectra. XLD is particularly evident in the ferroelectrically distorted TiO_6 environment of $Pb(Zr_{0.2}Ti_{0.8})O_3$, and is strongest near the t_{2g}-like feature in the L_3 edge (14). Calculations show that this t_{2g}-like feature is sharply sensitive to the angle between the ferroelectric axis and the X-ray polarization axis. Thus, the dichroism of this feature can be used to distinguish ferroelectric *a* domains from *c* domains.

In $PbTiO_3/SrTiO_3$ superlattices, the octahedral distortions are modulated by changes to the local electric polarization direction within the polar texture supercell, defined by the pair of clockwise and counterclockwise cores. Accordingly, the anisotropic dielectric response of each TiO_6 unit to resonant soft X-rays provides a contribution to the X-ray scattering amplitude that varies with polarization orientation. Fig. S1 shows schematically that, by approximating the TiO_6 octahedral distortions as rigid rotations, the anisotropic dielectric susceptibility tensor, χ_{ij}, undergoes a corresponding rotation (equivalent to a rotational change of basis). Combined with the phase delays from the translational offsets of individual TiO_6 units, the rotated anisotropic susceptibility results in a finite structure factor, F_{ij}, that generates ATS diffraction. The chiral helical structure in the lower left of Fig. S1 imparts a chiral structure factor onto the scattering amplitude, and will lead to XCD whose strength scales with the anisotropy of the ATS, χ_{ij}. This anisotropy is enhanced at the t_{2g}-like feature in the L_3 edge because of the periodic ordering of local electric polarization, which modulates between in-plane and out-of-plane orientations.

This is, in many ways, analogous to resonant ATS diffraction that occurs in materials that possess crystallographic screw axes (16). The combined effect of rotation and translation of the anisotropic atomic environment in materials such as α-quartz creates a finite structure factor and the appearance of "forbidden" diffraction peaks corresponding to the screw axis supercell. Off-diagonal transition elements are enhanced by dipole or multipole (*m* pole) resonant electronic transitions (15, 22), leading to polarization rotation of the reemitted X-rays (which depends on the projection angle of the incoming X-ray's polarization onto the primary axis of the transition *m* pole). Away from resonance, the ATS diffraction peaks vanish. Without sensitivity to anisotropy of the atomic sites with screw axis symmetry, these sites scatter identically so that the structure factor cancels for periods larger than the primary atomic cell governed by point group (rather than space group) symmetry.

At resonance, the ATS diffraction peaks for chiral materials can have a pronounced dependence on the polarization of incoming X-rays; in particular, they may exhibit XCD. For the screw axis operators that exist as chiral pairs (3_1, 3_2; 4_1, 4_3; 6_1, 6_5; 6_2, 6_4), the structure factors for many ATS diffraction peaks are also chiral (16). This occurs when two nonzero ATS elements are equal except for a $\pm\pi/2$ phase shift in the complex number plane (e.g., $F_{11} = \pm i\, F_{12}$). The chiral structure factors encode the incremental polarization rotation (due to resonant reemission) at successive *m*-pole scattering sites within the unit cell, effectively converting a linear anisotropy (XLD in the absorption/reemission process) into XCD for the diffraction peaks. As with the chiral crystal classes, the chiral electric polarization texture of the $PbTiO_3/SrTiO_3$ arrays generates a coherent superposition of chiral structure factors. In particular, the modulation of electric polarization within the central $(001)_\chi$ planes of each $PbTiO_3$ layer is helical, with a screw-like axis along the $[100]_\chi$ direction. A telltale feature of XCD in ATS diffraction from chiral structures is that the sign of the dichroism reverses when either the chirality of the crystal structure or the sign of the diffraction vector is independently inverted (16, 22–24).

Azimuthal XCD Measurements

In-plane anisotropy of the $DyScO_3$ $(110)_O$ substrate strongly favors polar cores ordered along the $[001]_O$ direction (core axes parallel to $[\bar{1}10]_O$), which is evident in planar view TEM and RSXD. However, as Fig. S10 shows, the polar textures do not exist exclusively in this orientation. A minority fraction orders along the orthogonal $[\bar{1}10]_O$ axis. The diffraction pattern (and XCD) generated by these orthogonal chiral domains is similar in every respect to the majority domains, other than the orientation of the diffraction spots (rotated azimuthally by 90°) and their absolute intensity (which is reduced due to the smaller volume fraction). We make use of this "redundancy" to collect data from multiple diffraction spots at a single orientation of the sample azimuth, Φ. This is illustrated in Fig. S10.

The azimuthal dependence of XCD in Fig. 3*A* is plotted versus ϕ_{spot}, rather than sample azimuth, Φ, to emphasize its symmetry. This visualization highlights how the XCD signal depends upon the relative orientation between the lateral ordering direction, $\pm[100]_\chi$, and the scattering plane defined by the incident X-rays and the detector (blue plane in Fig. 1*A*). That orientation is equivalent to measuring the in-plane angle, ϕ_{spot}, between $q_{lateral}$ and the projection of incident X-rays onto the sample surface (dashed green line in Fig. S10), because the diffraction vectors as defined here are fixed to the sample.

Resonance profiles collected at each azimuth were divided by I_0 and the preedge intensity (*RSXD Measurements*) and then, after subtracting the fluorescent background, normalized to the most intense feature in the polarization-averaged spectrum. Four ~200 × 200 pixel regions located away from significant diffraction features in all CCD images were used for background subtraction. The most intense XCD signal for each diffraction peak (in each case, measured near $\phi_{spot} = +90°$) was used to fit the XCD spectra at all other azimuths. To verify fits for consistency, fitting was performed both over the entire spectral range measured and also at only the L_3 edge; additionally, all fits were performed both weighted by the SD of the values obtained from multiple background regions and also unweighted. Error bars in the azimuthal plot (Fig. 3*A*) show the SD of these four fits applied to the dataset at each azimuth. Most data were captured at $n_{SL} = 4$, which has more accessible azimuthal values than $n_{SL} = 3$. Several points measured at $n_{SL} = 3$ are also included in Fig. 3*A*. Antisymmetric XCD in these diffraction spots is a result of the chiral texture being detected with opposite rotational sense.

Azimuthal XCD and Chirality

Chirality inferred from azimuthal XCD implies that the symmetry of the $PbTiO_3/SrTiO_3$ superlattices has been lowered by breaking the mirror symmetry along the lateral direction, $[100]_\chi$, in a similar manner for both $\Phi = 0°$ and 180°. Polar displacement maps extracted from HR-STEM cross-sections of the polar textures reveal significant buckling (Fig. S3), in which cores of the counterclockwise rotations lie at a different height than those of the clockwise rotations. Interestingly, the mere existence of the pairs of curled polar cores already seen in $PbTiO_3/SrTiO_3$ superlattices (5), even if buckled, is not a sufficient condition for chirality. Despite the broken mirror symmetry, Fig. S3*D* shows that chirality is precluded because a 180° rotation superimposes the mirrored image onto the original structure. Because chirality is forbidden for any structure in which the polarization is confined to a 2D plane, the chiral structure of the $PbTiO_3/SrTiO_3$ polar arrays must possess an additional axial component of polarization.

As discussed in the main text, the reversal of XCD polarity observed in Fig. 3*A* is a critical indicator of the chiral polarization texture of the arrays. A competing contribution to the XCD from dynamical effects might also be present, but the azimuthal pattern would be considerably different when these contributions

are dominant (19–21). Fig. S4*A* shows the azimuthal pattern of XCD from the (1/2, 0, −1/2) diffraction peak, corresponding to antiferromagnetic ordering in achiral CuO (20). Lobes of large positive XCD (red) are located symmetrically near $\psi = 120°$ to 140° and 300° to 320°; and lobes of large negative XCD (blue) are located symmetrically near $\psi = 40°$ to 60° and 220 °to 240°. Despite the splitting of XCD into positive and negative lobes, the azimuthal pattern of XCD dominated by dynamical effects retains twofold symmetry that is unlike the sign reversal in Fig. 3*A*. We note that magnetooptic polarization rotation plays a significant role in CuO, and that a contribution of similar origin does not exist in our system or the observed CD due to the lack of local magnetic moments in both $PbTiO_3$ and $SrTiO_3$.

Interestingly, the azimuthal pattern in Fig. 3*A* could be viewed as the summation of an antisymmetric pair of intensity lobes (corresponding to the chiral structure of the polar arrays) with a twofold pattern of primarily positive XCD arising from dynamical effects. This would explain why the azimuthal lobe of positive XCD is considerably larger than the lobe with negative XCD. The fine features in Fig. 3*A*, such as the reduction of XCD near 80°, and other asymmetric deviations could very well be driven by dynamical modulations. Similar features are observed in the azimuthal pattern of intensity for the (1/4, 1/4, 1/4) diffraction peak, corresponding to antiferromagnetic ordering in $LaNiO_3$ (21), measured with linearly polarized (σ, π) X-rays, that has been reproduced in Fig. S4*B*. While not a measure of XCD, this plot shows that dynamical effects (measured in asymmetric diffraction geometries similar to those used in our studies) produce (*i*) an intensity pattern with mirror symmetry that deviates slightly from twofold symmetry because intensity is shifted toward ψ near 120° and 240° (rather than 90° and 270°); as well as (*ii*) abrupt drops in intensity near $\psi = 90°$ and 270°. Our current analysis does not depend upon modeling these fine features but rather focuses on the general trend in Fig. 3*A* that positive XCD is observed at positive azimuths, while negative XCD is measured at negative azimuths.

RSXD Peak Shifts

Near resonant electronic transitions, strong changes to the complex optical index lead to dynamical scattering effects that can be observed, e.g., as shifts in the RSXD peak position (25). That is, the momentum transfer vector of the peak center changes as a function of photon energy. Near the Ti $L_{3,2}$ edges, we observe such shifts (Fig. S9*A*) for the $q_{lateral} = \pm q_{\chi\_pair}$ diffraction peaks at all four main absorption features (Fig. S9*B*). The magnitudes of these shifts are somewhat similar for all four absorption features. This indicates that resonant absorption and refraction should produce dynamical effects on the RSXD peaks that are comparable in magnitude near each absorption feature. However, XCD in the diffraction peak is strongly enhanced only near the L_3 t_{2g}-like feature (Fig. 1*C* and Fig. S9*C*) and therefore cannot be due purely to the dynamical effects of refraction. Moreover, the peak shifts show negligible dependence on the circular polarization of the X-rays. If XCD in the diffraction peak were primarily driven by refraction, one would expect polarization-dependent shifts in the peak position as well (21). These observations further demonstrate that XCD in the diffraction peak is indicative of the chiral texture in the polar arrays.

Second-Principles Calculations

Second-principles simulations of $PbTiO_3/SrTiO_3$ superlattices were carried out using the same superlattice potentials as in ref. 28. The interactions within the $PbTiO_3$ or $SrTiO_3$ layers were based on the previously introduced potentials for the bulk compounds, which give a qualitatively correct description of the lattice dynamical properties and structural phase transitions of both materials. For the interactions between ion pairs at the interface, simple numerical averages were used. For the periodicities of the superlattices studied in this work, the main effects of the stacking are purely electrostatic. Those long-range dipole−dipole interactions are governed by the Born effective charges of the bulk parent compounds and a bare electronic dielectric constant ε^{∞} that is taken as a weighted average of the first-principles results for bulk $PbTiO_3$ ($\varepsilon^{\infty,\,PTO} = 8.5$) and $SrTiO_3$ ($\varepsilon^{\infty,\,STO} = 6.2$) with weights reflecting the composition of the superlattice. To preserve the electrostatic interactions within each material as close as possible to the bulk parent compounds, we have rescaled the Born effective charge tensors of the inner atoms by $\sqrt{\varepsilon^{\infty}/\varepsilon^{\infty,ABO_3}}$ (where ABO_3 stands for $PbTiO_3$ or $SrTiO_3$, depending on the layer to which the atom belongs). In this way, following equation 24 of ref. 27, the dipole−dipole interactions remain the same as in bulk even if we adopt a common value of ε^{∞} for the whole heterostructure. The Born tensors corresponding to the atoms at the interfaces were left untouched.

Monte Carlo simulated annealings were used to induce structural relaxations and find the ground state or metastable solutions of the $2n \times n \times 2n$ elemental perovskite unit cells for the $n = 10$ superlattice. The starting point is from pure 180° Ising-like domains within the $PbTiO_3$ layers (where only the polarization along $[001]_{\chi}$ changes sign at the domain walls). Multiple local minima, essentially degenerate in energy but differing in the direction of the axial component, have been found. Some of them are characterized by a zig-zagged Z- (Fig. 5*A*) or S-shaped pattern (Fig. 5*C*) of the axial polarization component. Each Z (or S) region—or "axial domain"—contains one polar core and is terminated by extensions into the neighboring up and down domains at the interfaces with $SrTiO_3$. The Z (S) shape tilts the boundaries between axial domains to lie roughly along $\{101\}_{\chi}$ planes, across which both the axial component of polarization and the sense of core rotation reverse. These "axial domain walls" continue through both the $PbTiO_3$ and $SrTiO_3$ layers. The domain walls in $PbTiO_3/SrTiO_3$ superlattices are far from being of pure Ising type, instead presenting additional Néel-like and Bloch-like polarization components along $[100]_{\chi}$ and $[010]_{\chi}$, respectively.

The atomic configurations displayed in Fig. 5 *A* and *C* are chiral enantiomers (Fig. S6) whose symmetry is perfectly consistent with the observed azimuthal dependence of the XCD signal. Each structure contains a significant chiral component, for which the broken lateral $(100)_{\chi}$ mirror symmetry is unchanged by a 180° rotation. Fig. 3 *B* and *C* shows that a twofold rotation leaves unchanged the regions in proximity to the polar cores. Only within the up and down domains does the axial component of polarization reverse, i.e., axial Z domains become S domains. The 3D polarization near the cores is robust versus a twofold rotation, whereas this symmetry is absent outside of the cores due to reversal of the axial polarization. Opacity of the planar polarization arrows is scaled in Fig. 3*C* by the average local axial intensity. We emphasize that the shape of the axial domains (either S or Z) represents a degree of freedom in these structures that is independent from the chirality of the polar arrays.

Helicity of Calculated Polarization Textures

Helicity density (31) was computed from the local polarization structures (*Materials and Methods*) that were calculated by second principles. First, the local polarization vector is normalized at every place in space. Then spatial derivatives are computed from finite differences, and the curl is calculated locally at every position. Since the curl of the polarization essentially vanishes at the center of the up and down domains, the helicity density takes nonzero values only in a region surrounding the polar cores (Fig. 5 *G–I*), where the axial component of the polarization is essentially constant (the surrounding up and down domains contribute

only marginally to the helicity, and could be responsible for quantitative variations in the azimuthal XCD measurements). The curl points along the axial direction, and its sign depends on the sense of the polarization rotation. Therefore, the sign of the helicity density of a polar core depends on whether the direction of the curl is parallel ($\gamma > 0$) or antiparallel ($\gamma < 0$) to the axial component of the polarization.

Fig. S1 shows that the central $PbTiO_3$ layers contain a helical structure similar to Fig. 2*A*. This lateral helix is inextricably linked to the helicity number, both of which would reverse if the axial polarization were inverted. As such, the helicity number and the lateral helix can be considered two ways of viewing the same alternating axial polarization of the cores located between the alternating up and down domains.

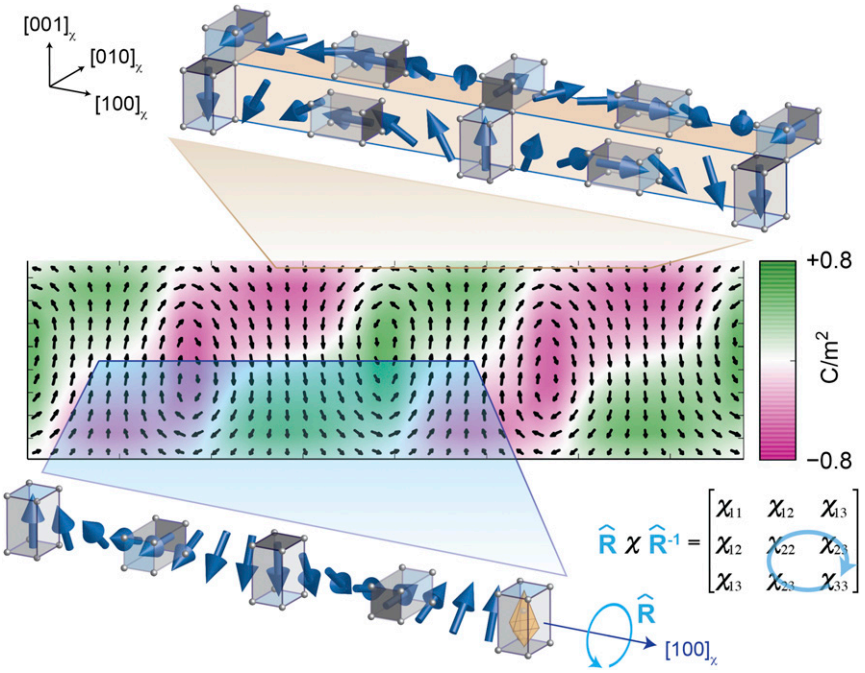

Fig. S1. Rotational textures of electric polarization produce ATS diffraction from chiral polar arrays. The complex polarization texture of the $PbTiO_3/SrTiO_3$ arrays contains multiple subtextures that exhibit periodic rotation of the electric polarization along $[100]_\chi$. Two subtextures are schematically depicted as line cuts extracted from the polarization map of the $PbTiO_3$ layer. The polarization map was calculated by second principles, where the meaning of the arrows and color levels is the same as in Fig. 5. Conical blue arrows show a helical rotation of polarization near the central atomic planes (blue) similar to chiral Bloch domain walls. Near the interfaces with $SrTiO_3$ (beige), the primarily Néel character shows cycloidal rotation of the polarization. The rotated polar units can be approximated as a rigid rotation of distorted TiO_6 octahedra. Rotation ($\hat{R}$) of this anisotropic local environment is accompanied by a rotational change of basis to the anisotropic dielectric susceptibility tensor (χ_{ij}). Diffraction from the periodic chiral modulation to the anisotropy of the titanium local environment within the polar texture supercell produces XCD.

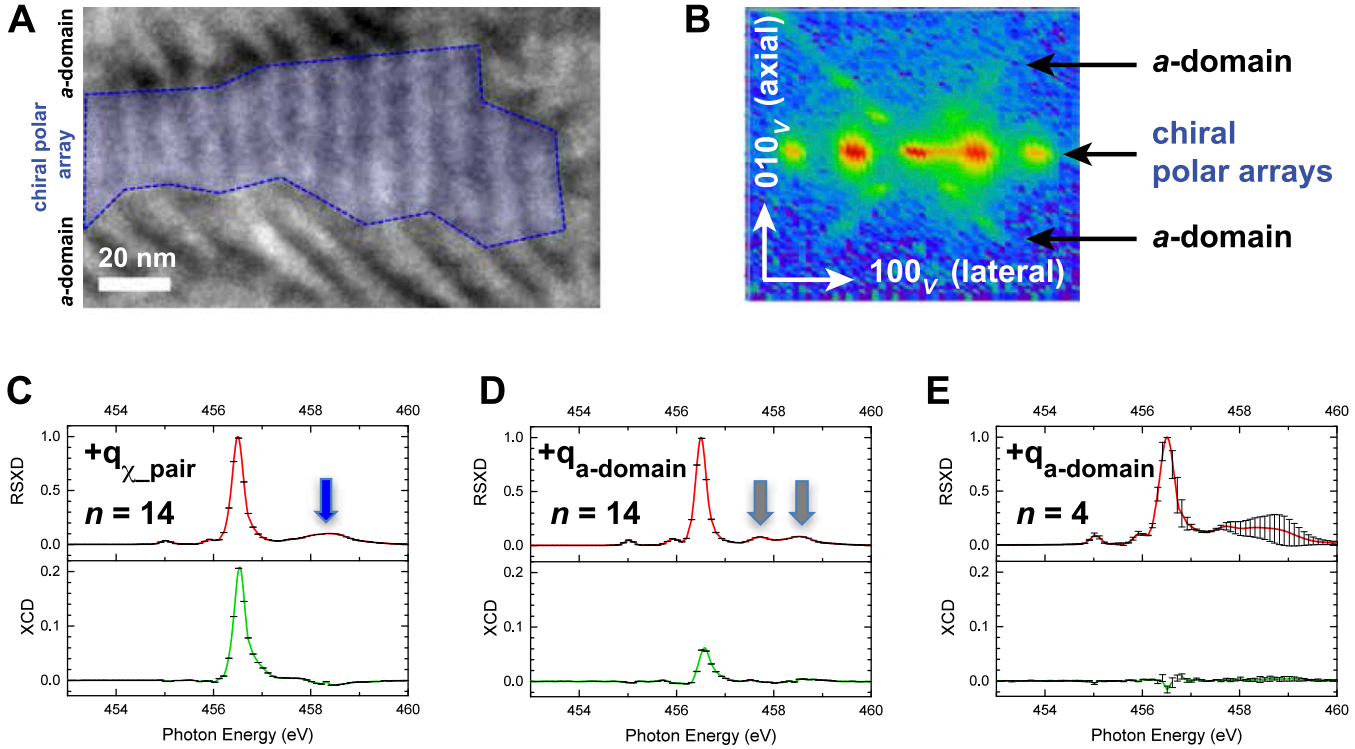

Fig. S2. Distinguishing RSXD signal of chiral polar textures from diffraction signal of *a* domains. (*A*) Planar view TEM images show that regions of chiral polar arrays (vertical stripes) coexist next to regions of a_1/a_2 domains (diagonal stripes). (*B*) X-rays scattered from chiral polar arrays produce diffraction spots (arranged horizontally here) distinct from the (diagonal) diffraction spots of periodically ordered *a* domains. There is sufficient separation (and instrumental resolution) in reciprocal space to isolate the various diffraction spots at the soft X-ray photon energies used in this study. Ti L_3 resonance profiles of the (*C*) chiral polar texture and (*D*) *a*-domain diffraction spots are similar but not identical in an $n = 14$ superlattice. The *a*-domain resonance in *D* shows substantial splitting of the e_g feature (arrows), not seen in the e_g feature of the chiral texture resonance *C* (arrow). The resonance profile in *C* shows a significant (~20%) XCD indicative of the chiral polar arrays. A residual, small XCD is present in the *a*-domain spectrum in *D*, although it is considerably smaller than that of the chiral texture in *C*. (*E*) By comparison, the resonance profile of the *a*-domain diffraction spot in an $n = 4$ superlattice (in which chiral order is not present) shows XCD that is essentially negligible.

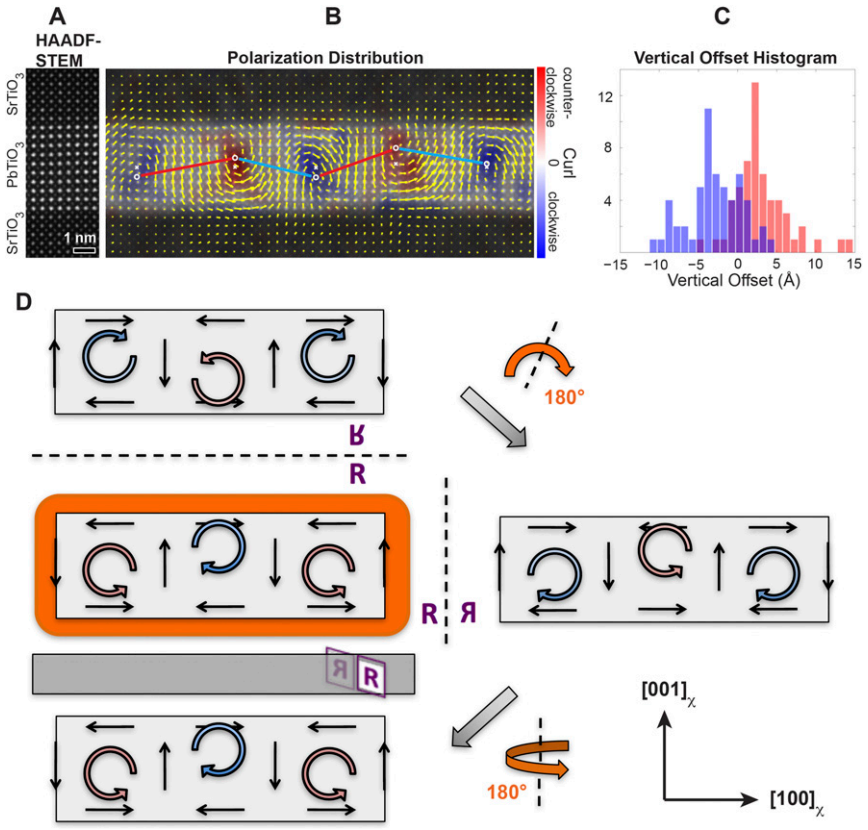

Fig. S3. Buckling of curled polarization cores observed in polar displacement maps extracted from HR-STEM cross-sections. (*A*) Cross-sectional HR-STEM high-angle annular dark-field (HAADF) image of an $n = 10$ superlattice showing sharp interfaces between $PbTiO_3$ and $SrTiO_3$. (*B*) Polar atomic displacement map showing components of electric polarization within the $(010)_\chi$ plane that define the curled polarization texture. The local curl vector, $\vec{\nabla} \times \vec{p}$, is color-coded to indicate clockwise (blue) and counterclockwise (red) rotation. The center of each core is indicated by a white circle and connected by zig-zagged lines to highlight the buckling of cores that is typically observed. (*C*) Quantitative analysis of the positions of 56 pairs of cores shows a split distribution, with counterclockwise cores residing ~5 Å higher than their clockwise counterparts. (*D*) A purely 2D electric polarization texture, even for an array with buckled cores, is not chiral. Three orthogonal reflections of the polar texture supercell are examined. The original cell is outlined in orange (*Middle Left*), and polarization components are constrained to the $(010)_\chi$ plane. Clockwise and counterclockwise cores are represented schematically by arrows indicating the direction of electric polarization. Reflected images are shown for three mirror planes: (*Upper Left*) $(001)_\chi$, (*Middle Right*) $(100)_\chi$, and (*Lower Left*) $(010)_\chi$. *Upper Left* can be mapped onto *Middle Right* by a 180° rotation around $[010]_\chi$. *Middle Right* can in turn be mapped onto *Lower Left* by a 180° rotation around $[001]_\chi$. *Lower Left* is identical to the original supercell; by definition, this configuration is not chiral.

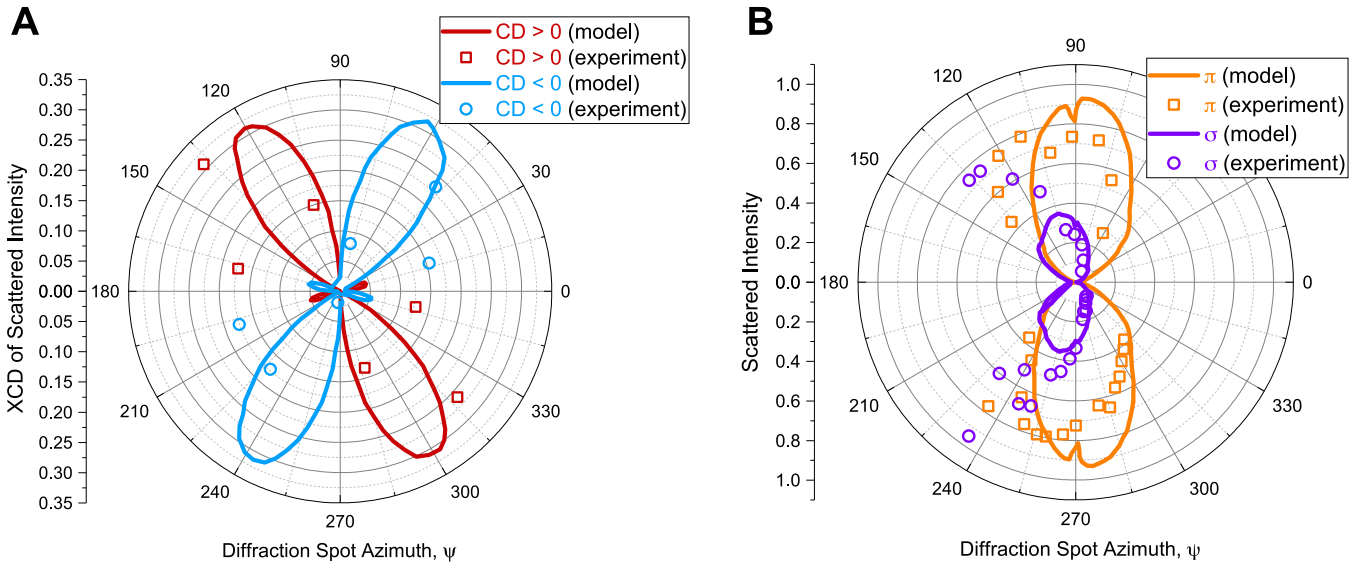

Fig. S4. Azimuthal symmetry of dichroism in RSXD dominated by dynamical effects. (*A*) XCD measured at (1/2, 0, −1/2) diffraction peak in CuO, corresponding to antiferromagnetic order; data are reproduced from ref. 20. (*B*) Intensity of (1/4, 1/4, 1/4) antiferromagnetic ordering diffraction peak in $LaNiO_3$, measured with linearly polarized (σ, π) X-rays; data are reproduced from ref. 21.

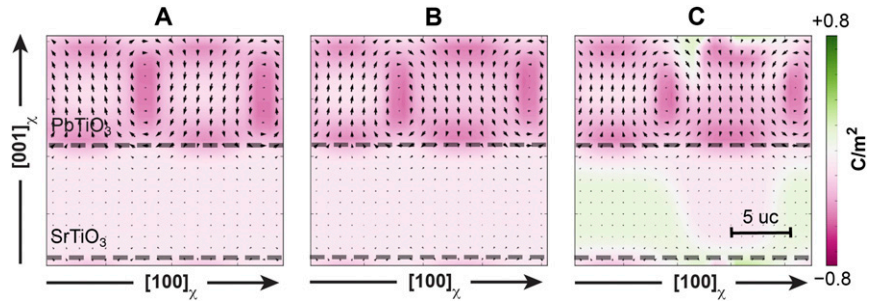

Fig. S5. Stability of chiral polar texture calculations vs. simulation cell size. Second-principles simulations on superlattices with different lateral sizes along $[100]_\chi$ show how the lateral period of clockwise and counterclockwise pairs theoretically predicted is essentially independent of the simulation cell. The lateral dimension of each simulation cell contains (*A*) 18, (*B*) 20, or (*C*) 22 elemental perovskite unit cells, with periodic boundary conditions applied. Simulations have been carried out at $T = 10$ K. Meaning of the arrows and color levels are the same as in Fig. 5.

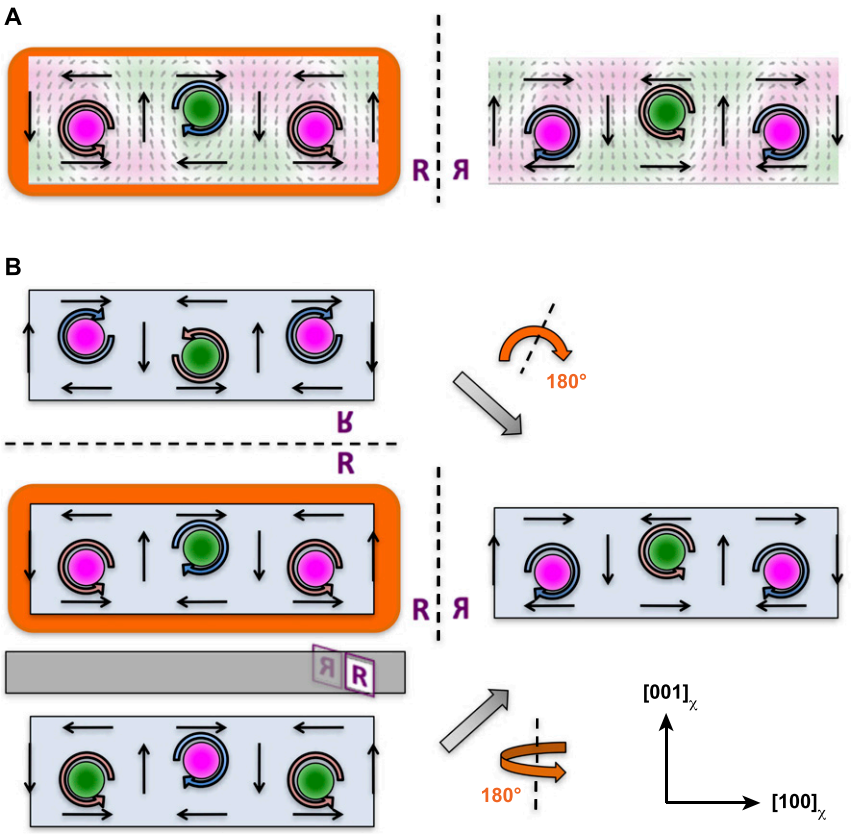

Fig. S6. Chirality of simulated 3D electric polarization texture. (*A*) Calculated polarization textures from Fig. 5 *A* and *C*, with arrows and color levels having the same meaning. Key features of the chiral texture are schematically overlaid. Clockwise and counterclockwise cores are represented by arrows indicating the direction of electric polarization; opposite directions of axial polarization near the cores are indicated by green and magenta shading. (*B*) Three orthogonal reflections of the chiral texture supercell are examined. The original cell is outlined in orange (*Middle Left*). Reflected images are shown for three mirror planes: (*Upper Left*) $(001)_\chi$, (*Middle Right*) $(100)_\chi$, and (*Lower Left*) $(010)_\chi$. *Upper Left* can be mapped onto *Right* by a 180° rotation around $[010]_\chi$. Additionally *Lower Left* can be mapped onto *Middle Right* by a 180° rotation around $[001]_\chi$. The reflected images all map onto one another but cannot be mapped onto the original structure by any combination of rotations and/or translations because they are chiral enantiomers.

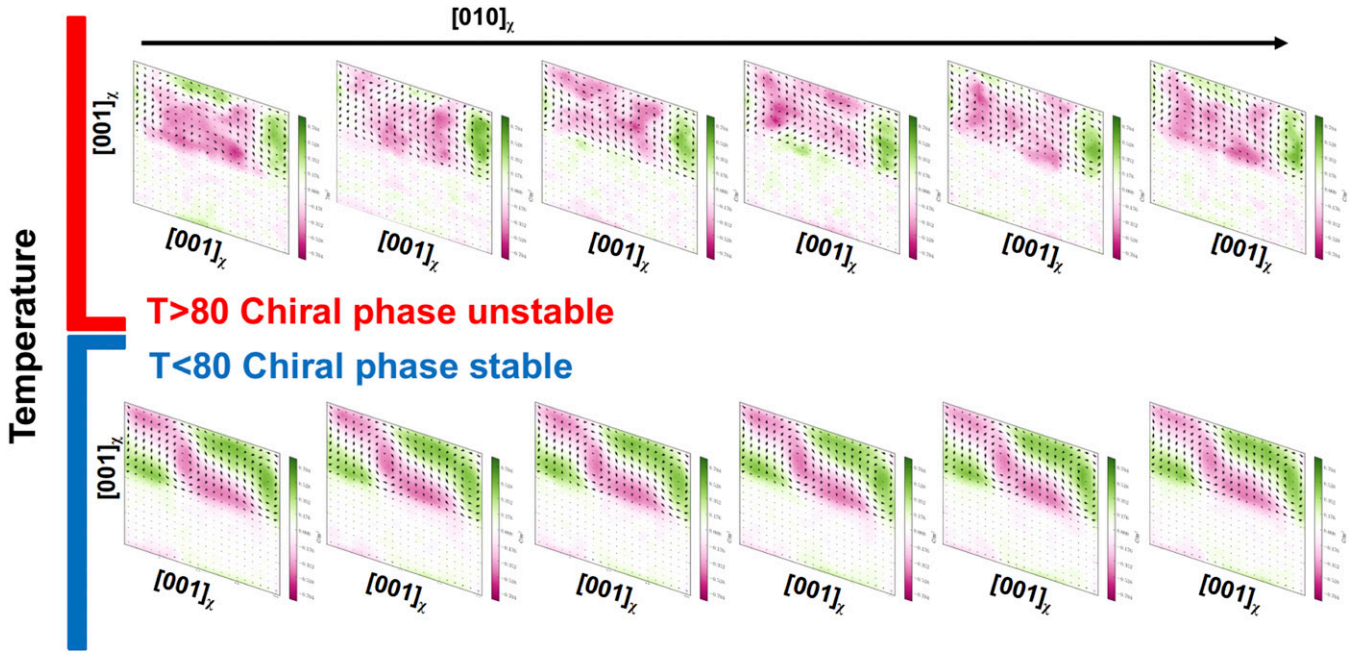

Fig. S7. Stability of the chiral polar textures with the temperature from second principles. The local polarization is plotted for successive $(010)_\chi$ planes of the simulation box for (*Upper*) $T = 85$ K and (*Lower*) $T = 10$ K. At high temperature, thermal fluctuations allow local flipping of some dipoles, and the domain walls change their shape from one plane to the next. The average value of the polarization, especially the axial component, is reduced. At low temperature, the domain walls are preserved throughout the structure. Meaning of the arrows and color levels are the same as in Fig. 5.

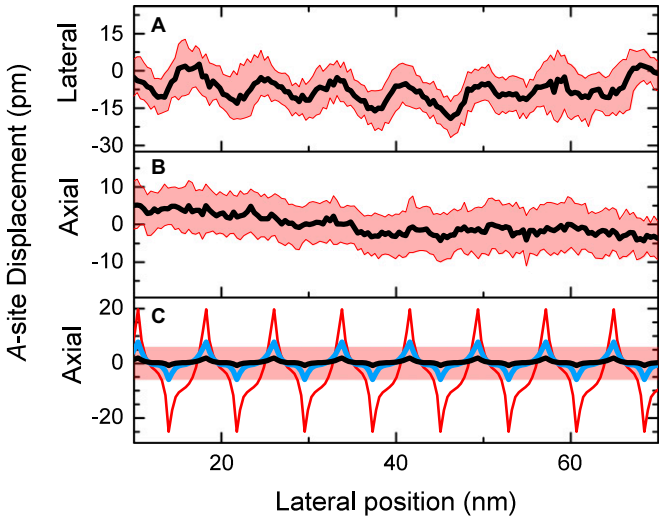

Fig. S8. In-plane electric polarization components extracted from HR-STEM, averaged through depth of $PbTiO_3/SrTiO_3$ film stack. Atomic shifts of the *A*-site cations (e.g., Pb or Sr) relative to a reference grid were extracted from planar view HR-STEM images of $PbTiO_3/SrTiO_3$ multilayers. Atomic shifts corresponding to components of electric polarization along the (*A*) lateral $[100]_\chi$ and (*B*) axial $[010]_\chi$ directions are shown as 1D line cuts along the $[100]_\chi$ direction. A clear modulation of the lateral component is observed in *A* despite the sizeable band of uncertainty (red regions show 25th to 75th percentile) due to noise in the measurement. These planar view HR-STEM measurements reflect the depth-averaged value through all layers. (*C*) Axial *A*-site displacements from second-principles simulations, calculated at midheight of the $PbTiO_3$ layer (red), depth-averaged for the $PbTiO_3$ + $SrTiO_3$ layers (blue), and depth-averaged to match the thickness of the TEM sample in *A* and *B*, which includes ~50 nm substrate (black). The shaded region of *C* shows that the modulated axial component in the latter lies within the band of uncertainty for the HR-STEM measurement in *B*.

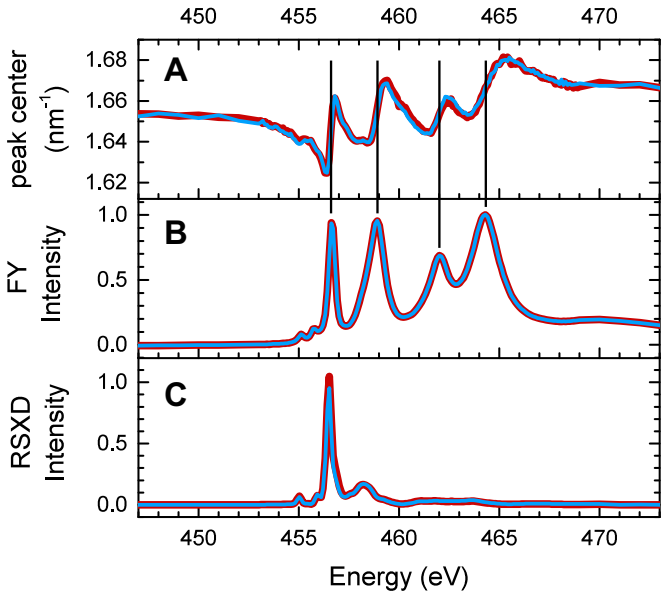

Fig. S9. Shift in RSXD peak position due to dynamical scattering effects. (*A*) Out-of-plane momentum transfer (component parallel to $[001]_\chi$) and (*C*) RSXD intensity of the n_{SL} = 3 chiral array diffraction peak at $q_{lateral} = +q_{\chi\_pair}$ plotted versus photon energy. (*B*) Fluorescence yield (FY) spectrum of absorption intensity. Data measured using right- (red) and left-circularly (blue) polarized X-rays for an n = 14 superlattice. Vertical black lines show that "derivative-shaped" peak shifts in *A* are centered at the absorption peaks in *B*.

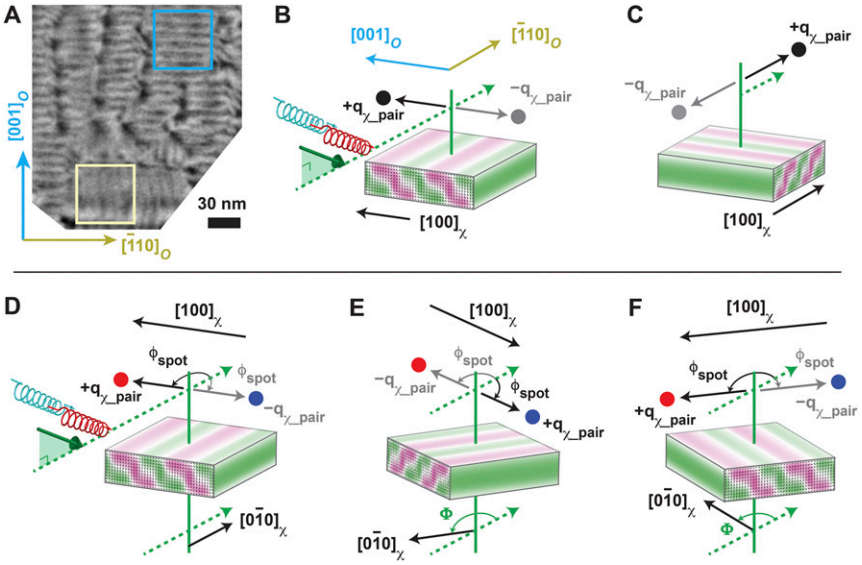

Fig. S10. Azimuthal positions of diffraction spots from chiral polar arrays—aligned along majority orientation or minority orientation—are defined relative to incident X-ray beam. (*A*) Planar view TEM images show that the majority of chiral polar arrays (horizontal stripes in blue square) are ordered along the $[001]_O$ direction of the $DyScO_3$ $(110)_O$ substrate while a minority (vertical stripes in yellow box) are ordered along $[\bar{1}10]_O$. (*B*) In this sample orientation, the horizontal stripes produce a pair of diffraction spots along the $[001]_O$ ordering direction. (*C*) The minority vertical stripes instead produce a pair of diffraction spots along the $[\bar{1}10]_O$ ordering direction, albeit with lower intensity. Geometrical quantities important to the diffraction experiments are shown for three orientations of the sample azimuth, Φ: (*D*) 0°, (*E*) 158°, and (*F*) 67°. Φ is the angle between $[0\bar{1}0]_\chi$ and the in-plane projection (dashed green arrow) of the incident X-ray beam (solid green arrow). Curved arrows indicate the azimuth of each diffraction spot, ϕ_{spot}, measured between the in-plane projection of the diffraction vector ($q_{lateral}$) and the same reference used for Φ. The projection of the chiral array diffraction vector onto $[100]_\chi$ determines whether $q_{lateral} = +q_{\chi\_pair}$ (black arrow) or $q_{lateral} = -q_{\chi\_pair}$ (gray arrow). The measured polarity of XCD is indicated for each diffraction vector as a solid red (XCD > 0) or blue (XCD < 0) circle.